JOURNAL OF AIRCRAFT
Vol. 43, No. 1, January–February 2006

Accurate Drag Prediction Using Cobalt

Kenneth E. Wurtzler*
Cobalt Solutions, LLC, Dayton, Ohio 45504
and
Scott A. Morton†
U.S. Air Force Academy, Colorado Springs, Colorado 80840

The technical objective of the Second AIAA Computational Fluid Dynamics (CFD) Drag Prediction Workshop is to assess the state-of-the-art computational methods as practical aerodynamic tools for aircraft force-and-moment prediction of increasingly complex geometries. With more emphasis being placed on CFD methods to evaluate aircraft designs early in the design process, the ability to accurately predict the forces and moments, specifically drag, on an airliner configuration is important. Using the CFD code Cobalt, force-and-moment calculations are obtained on a civil transport geometry with and without engine nacelle and pylon.Comparisons with experimental data show consistent agreement with forces and moments, wing *Cp* data, and qualitative data. Installation drag for the nacelle/pylon is well predicted. Relevance of the importance of the grid and robustness of the flow solver to the overall accuracy of the results is discussed.

Nomenclature

c = wing-root chord, 14.1 cm
M = Mach number, 0.75
Re = Reynolds number, $U_\infty c/\upsilon_\infty$
α = angle of attack

Introduction

GOVERNMENT and university labs and the aircraft industry have been developing computational methods suitable for aircraft loads prediction for decades. Only recently have computer codes been available that can provide accuracy and robustness for general geometries at flight Reynolds numbers. In an effort to document the degree to which current computational-fluid-dynamics (CFD) codes can predict the loads of a generic configuration, the AIAA sponsored the Second CFD Drag Prediction Workshop in June of 2003. The technical objective was to assess the state-of-the-art computational methods as practical aerodynamic tools for aircraft force-and-moment prediction of increasingly complex geometries and to build on the results of the First Drag Prediction Workshop by investigating incremental drag as well as total drag. Special emphasis was placed on drag prediction accuracy and component drag increments. A secondary objective was to identify areas needing additional research and development.

To meet these objectives, the workshop provided a common geometry and reliable, available, test data for comparison. The complete workshop case list included a single-point grid-convergence study, drag polar, fully turbulent vs tripped boundary layer, and drag rise computations.

For CFD tools to be useful, they must act as a predictive method with little reliance on previous design data. Aircraft designs that progress with little geometric difference provide an easy method to "calibrate" CFD codes. Results are adjusted according to the error from the previous design result. The force-and-moment data that this calibration process provides might not be consistent with the flow physics. Therefore, this process is unreliable in the face of unsteady flow phenomena such as shock/boundary-layer interaction and separation. It also cannot be used for radical new designs and flight regimes that have no database of force-and-moment data associated with it.

It is also important to maintain the geometric integrity so as to provide for a precise comparison with the wind-tunnel results. Modifying the geometry according to previous computational results removes the predictive capability of CFD for new designs. Any modification also introduces unknown error into the solution.

Accurate force-and-moment prediction must also be consistent across all forces and moments. This will ensure the correct pressure distribution for the lift is obtained around the aircraft. It will also enable better prediction of installation drag along with prediction of the absolute force values. The current work seeks to demonstrate the ability of the computer code Cobalt to provide these accurate simulations of a generic airliner configuration.

Computational Method

Cobalt is a commercial hybrid Navier–Stokes flow solver. Cobalt is highly robust and accurate and possesses great parallel performance. Cobalt solves the Navier–Stokes equations, including an improved spatial operator and improved temporal integration. The code has been validated on a number of problems.[1] Tomaro et al. converted Cobalt from explicit to implicit, enabling Courant–Friedrichs–Lewy numbers as high as one million.[2] Grismer et al. then parallelized the code, yielding a linear speedup on as many as 1024 processors.[3] Forsythe et al. provided a comprehensive testing and validation of the Reynolds-Averaged Navier–Stokes models, including the Spalart–Allmaras, Wilcox k-ω, and Menter's shear stress transport turbulence models.[4]

The numerical method is a cell-centered finite volume approach applicable to arbitrary cell topologies, for example, hexahedra, prisms, and tetrahdra. The spatial operator uses the exact Riemann solver of Gottlieb and Groth,[5] least-squares gradient calculations using QR factorization to provide second-order accuracy in space, and total variation diminishing flux limiters to limit extremes at cell faces. A point implicit method using analytic first-order inviscid and viscous Jacobians is used for advancement of the discretized system. For time-accurate computations, a Newton subiteration scheme is employed, and the method is second-order accurate in time.

Grids

The computational grids were created using the software programs Gridtool[6] to develop the surface point distributions and background sources, and VGRIDns[7] to create the volume grid. The outer dimensions of the computational domain were

Presented as Paper 2004-395 at the AIAA 42nd Aerospace Sciences Meeting and Exhibit, Reno, NV, 5–8 January 2004; received 25 February 2004; revision received 24 June 2004; accepted for publication 2 July 2004.

*Vice President, Department of Marketing.
†Professor, Department of Aeronautics.

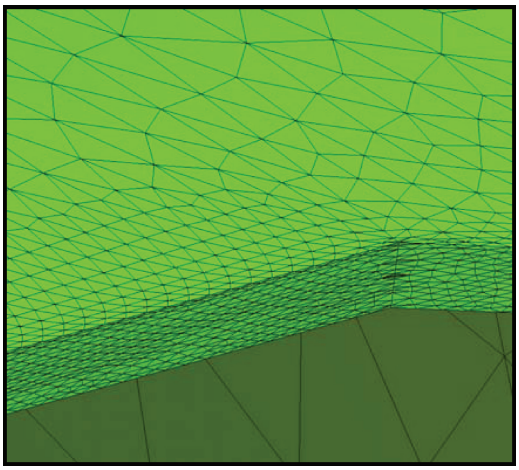

Fig. 1 Fine grid wing/trailing-edge surface mesh.

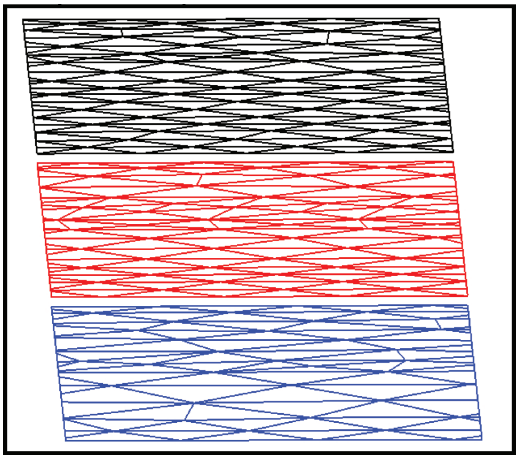

Fig. 2 Trailing-edge surface grid of the fine (top), medium (middle), and coarse (bottom) grids.

850 cm $< X <$ 850 cm (streamwise), 0 cm $< Y <$ 700 cm (spanwise), -450 cm $< Z <$ 450 cm (surface normal), where the wing-root chord is 14.1 cm. A half-span assumption was made for all grids generated. Initially, for the wing-body and wing-body-nacelle-pylon configurations, three grids were constructed to complete a grid-resolution study (coarse, medium, and fine).

The initial grids for the wing/body and wing/body/nacelle/pylon configurations were created with surface triangles concentrated on the leading edge and trailing edge. Surface triangles on the upper and lower wing surface were stretched by a factor of 1.5. The trailing edge had a thickness to it, and much attention was paid to placing the proper number of cells across the edge (Fig. 1).

The fine grid had approximately 30 cells across the trailing edge with the medium and coarse grids having less (Fig. 2).

Because the trailing-edge area is of very high aspect ratio, the cells on that particular surface were stretched and also had a high aspect ratio. This was necessary to avoid an impossibly high number of cells if no stretching was used. The stretching factor for the trailing-edge cells for the fine grid was on the order of four. It was also difficult to maintain a smooth distribution of cells across the trailing edge. The distribution of surface triangles for the wing/body grids is shown in Table 1, and the wing/body/nacelle/pylon grids is shown in Table 2. The emphasis of cells on the trailing edge is obvious from Tables 1 and 2, with the smallest area of the listed components (the trailing edge) having the first or second largest number of triangles on its surface.

The grids for the grid-resolution study were generated by changing the ifact value in VGRIDns. This value globally scaled the distribution of points on the surface and in the volume grid creating a set of grids consistently more refined in all three coordinate directions. The final grid output from VGRIDns was comprised solely of tetrahedral cells. The grid utility Blacksmith was used to combine tets in the boundary layer into prisms. Each layer created only contained prisms—there were no mix of prisms and tets in a layer. This process reduced the overall numbers of cells and also created higher quality cells in the boundary layer. The value of ifact, number of surface triangles, and resultant grid size for the wing/body geometry and the wing/body/nacellel/pylon geometry are shown in Tables 3 and 4, respectively.

Adaptive mesh refinement was performed using a version of VGRIDns. Pirzadeh[8] presented a method based on a tetrahedral unstructured grid technology developed at NASA Langley Research Center with application to two configurations with vortex-dominated flowfields. The mesh refinement only occurred outside of the boundary layer, and the fine grid was chosen as the start for both WB and WBNP geometry because it had the highest quality surface grid. A flow solution was computed for the fine grid just described, and the solution was used to create an AMR grid by eliminating all cells within an isosurface of vorticity at a particular level. The tetrahedral grid was then grown inside of the isosurface with an ifact of 0.6.

Table 1 Distribution of surface triangles for wing/body geometry

Surface	Fine grid	Medium grid	Coarse grid
Upper wing	63,075	48,839	38,660
Lower wing	61,499	46,284	38,625
Trailing edge	62,437	48,138	38,963
Wing tip	2,531	1,891	1,516
Fuselage	10,591	8,082	6,377

Table 2 Distribution of surface triangles for wing/body/nacelle/pylon geometry

Surface	Fine grid	Medium grid	Coarse grid
Upper wing	63,075	48,839	38,660
Lower wing	61,499	46,284	38,625
Trailing edge	62,437	48,138	38,963
Wing tip	2,531	1,891	1,516
Fuselage	10,591	8,082	6,377
Nacelle	40,351	30,589	24,237
Pylon	9,036	6,889	5,438

Table 3 Wing/body grids with surface triangles and grid size

Grid	ifact value	Description
Coarse	1.30	122,141 surface triangles 5,268,540 tets 3,802,848 tets/prisms
Medium	1.15	153,234 surface triangles 6,714,822 tets 4,876,014 tets/prisms
Fine	1.0	200,133 surface triangles 8,975,988 tets 6,574,392 tets/prisms

Table 4 Wing/body/nacelle/pylon grids with surface triangles and grid size

Grid	ifact value	Description
Coarse	1.30	139,600 surface triangles 6,114,050 tets 4,718,050 tets/prisms
Medium	1.15	175,550 surface triangles 7,797,527 tets 6,042,027 tets/prisms
Fine	1.0	232,572 surface triangles 10,528,768 tets 8,202,958 tets/prisms

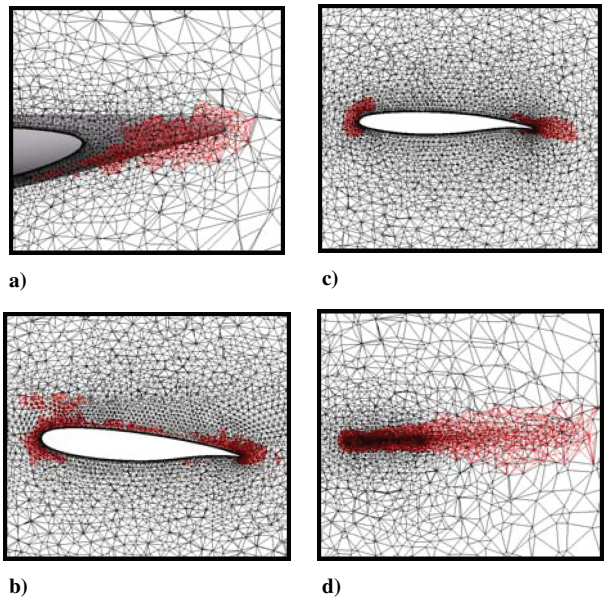

Fig. 3 Comparison of grid density at span stations a) 0.5, b) 0.8, c) 2.2, and d) wing tip.

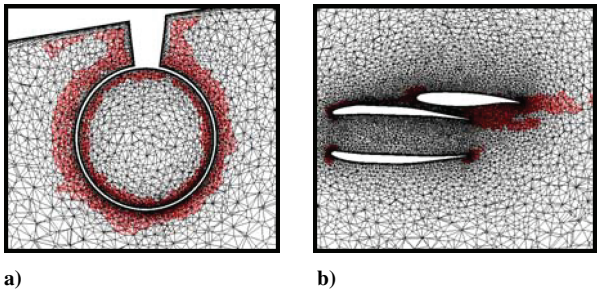

Fig. 4 Comparison of grid density a) aft of nacelle and b) inboard of pylon.

A comparison of the original grid and the AMR grid for the wing-body (WB) geometry is shown in Fig. 3 and for the wing-body-nacelle-pylon adapted grid (WBNP) geometry in Fig. 4. The red region is the adapted region inside of the isosurface. Outside of the adapted region, the grids are equivalent. The adapted WB grid has 8,083,504 cells, and the adapted WBNP grid has 8,872,611 cells.

All of the grids in this study consist of an inner region of approximately eight layers of prisms for the boundary layer, with a wall-normal spacing in viscous wall units less than one, and an outer region of tetrahedra. The prism dimensions on the surface were a factor of approximately 200 times larger than the wall normal dimension for all grids.

Results

The single-point convergence study and the drag polar portion of the drag prediction workshop are presented and discussed for the WB and WBNP geometries. WB solutions were run for 500 iterations, and the WBNP solutions were run for 1000 iterations, starting from freestream conditions. Typical convergence data for the wing-body fine grid are shown in Fig. 5. Menter's SST turbulence model was used for all calculations.

Initially, solutions were computed for various grids at a 0.49-deg angle of attack consistent with the angle of attack the experiment reported $C_L = 0.5$. Next, solutions for an angle of attack of 0 deg were computed, and interpolation was used to determine the computed angle of attack corresponding to $C_L = 0.5$. A solution was run at this angle of attack to verify the value of C_L. Finally, a range of angles of attack were computed, and the C_L, C_D, and C_M values reported for the WB and WBNP configurations. All of the solutions in the single point and drag polar studies were for $M = 0.75$, $Re = 3 \times 10^6$, and a fully turbulent assumption. Comparisons were made with wind-tunnel force-and-moment data and pressure data.

Table 5 Single-point data for the fine and adapted grids at $\alpha = 0.49$ deg for the wing-body case

Force/moment	Experimental	Cobalt	% Diff
C_L	0.4984	Fine 0.5190	3.9
		Ad 0.5142	3.2
C_D	0.0294	Fine 0.0302	2.6
		Ad 0.0301	2.3
C_M	−0.1213	Fine −0.1185	2.4
		Ad −0.1170	3.5

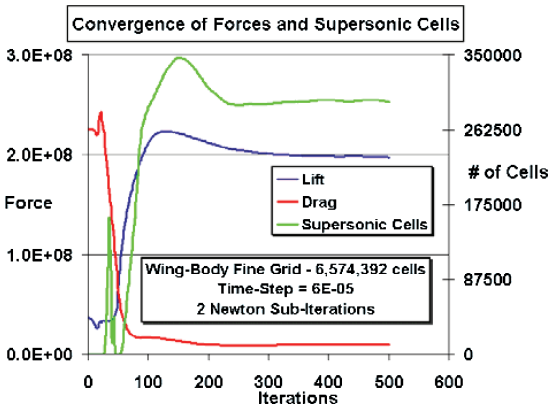

Fig. 5 Convergence for the wing-body fine grid at $\alpha = 0.49$ deg.

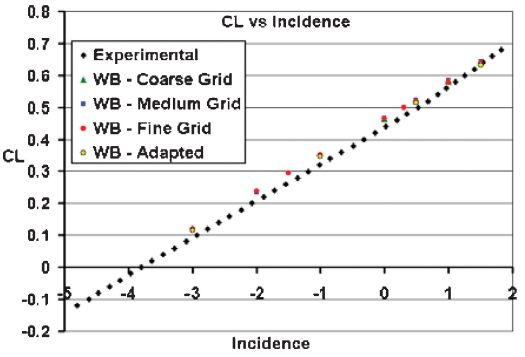

Fig. 6 Plot of C_L vs incidence for the wing-body geometry.

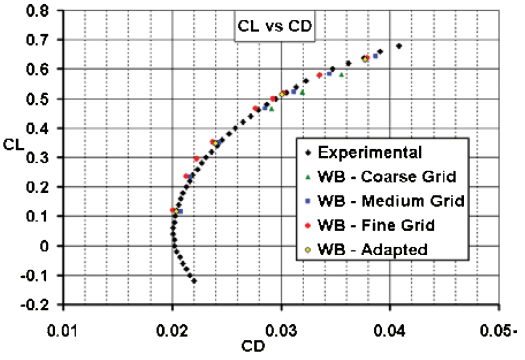

Fig. 7 Plot of C_L vs C_D for the wing-body geometry.

The WB single-point comparison data for the fine and adapted grids at $\alpha = 0.49$ deg is presented in Table 5. The experimental α for $C_L = 0.50$ is 0.49 deg, and the computationally predicted α is 0.31 deg.

Figures 6–8 depict the C_L, C_D, and C_M values at a range of angles of attack for the experiment and the computed results. All three

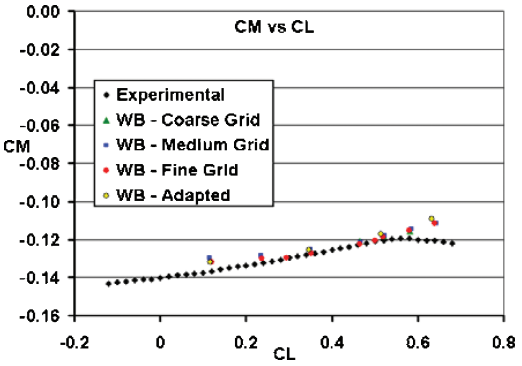

Fig. 8 Plot of C_M vs C_L for the wing-body geometry.

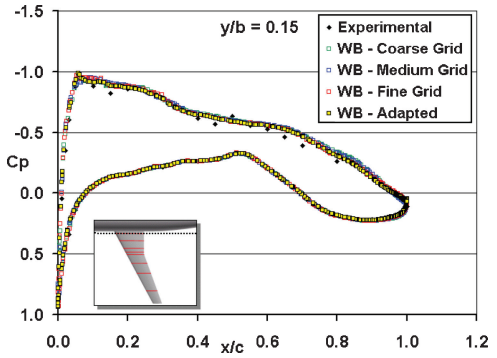

Fig. 9 *Cp* plot at $y/b = 0.15$, $\alpha = 0.49$ deg.

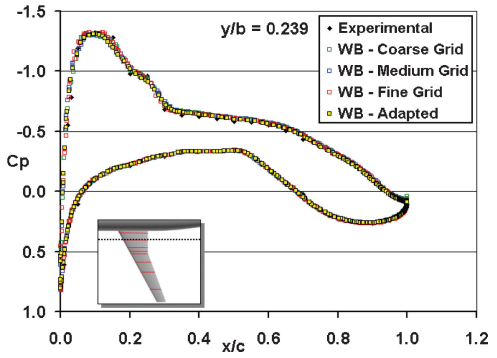

Fig. 10 *Cp* plot at $y/b = 0.239$, $\alpha = 0.49$ deg.

figures demonstrate improvement of the experimental comparisons with grid refinement. The drag-and-moment curves show the largest improvement, whereas the lift curve is only slightly improved with grid refinement. The adapted grid shows the best comparison with experiment for C_L, C_D, and C_M, and shows evidence of a grid-converged solution. All three curves show consistent trends with α, matching slopes for C_L and C_M, and quantitative matches of C_L, C_D, and C_M within 5% for all angles of attack in the linear regime. Only values of C_M corresponding to C_L greater than 0.5 show some deviation from experimental trends. Although all solutions were run with numerical parameters consistent with steady state, there were regions of separated flow observed that could necessitate unsteady time averages be computed, especially at the higher angles of attack.

To ensure that the integrated quantities of lift, drag, and pitching-moment comparisons were not fortuitous, quantitative analysis of the surface pressures at various spanwise chord lines was accomplished at an angle of attack of 0.49 deg, where experimentally obtained pressure coefficient data were available.

Figures 9–14 depict the C_p data at various spanwise stations for the $\alpha = 0.49$ deg case. Good agreement between the computations and experiments are observed for all spanwise stations. There appears to be little difference between the three refined grids and the

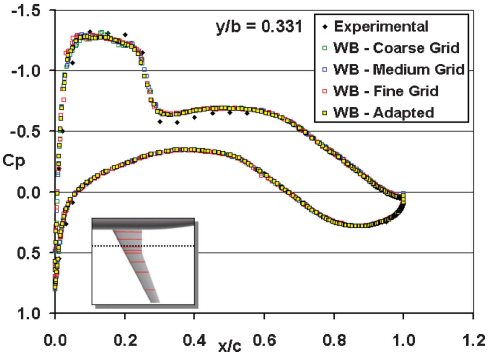

Fig. 11 *Cp* plot at $y/b = 0.331$, $\alpha = 0.49$ deg.

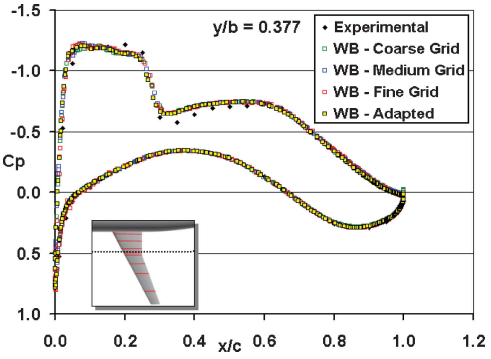

Fig. 12 *Cp* plot at $y/b = 0.377$, $\alpha = 0.49$ deg.

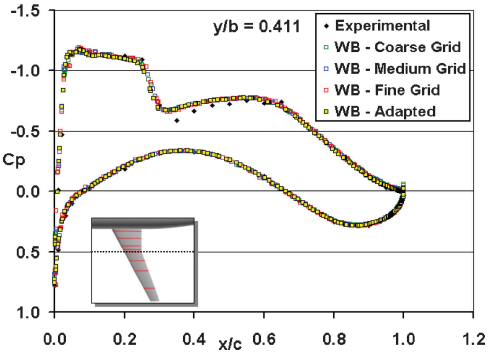

Fig. 13 *Cp* plot at $y/b = 0.411$, $\alpha = 0.49$ deg.

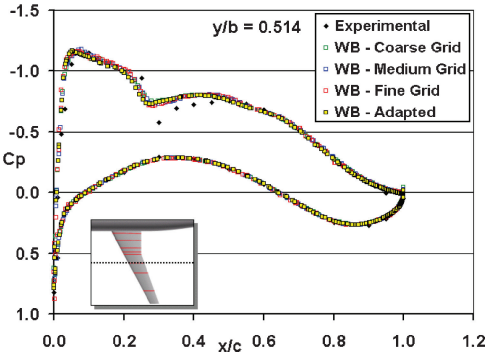

Fig. 14 *Cp* plot at $y/b = 0.514$, $\alpha = 0.49$ deg.

adapted grid. The adapted grid does predict the shock location better and lower C_p values on the upper wing aft of the shock.

A qualitative view of the flow at $\alpha = 0.49$ deg is shown in Figs. 15 and 16. The separated region at the wing root on the upper side, shown in red in Fig. 14, was documented in the wind tunnel. However, the narrow separated region along the trailing edge has a much greater impact on integrated forces and moments. This separation is three-dimensional because of the isosurface calculation factors

Table 6 Single-point data for the fine and adapted grids at $\alpha = 1.00$ deg for the wing- body-nacelle-pylon case (computational results are from the fine grid)

Force/moment	Experimental	Cobalt	% Diff
C_L	0.5005	Fine 0.5124	2.4
		Ad 0.5140	2.7
C_D	0.0338	Fine 0.0338	0
		Ad 0.0338	0
C_M	−0.1199	Fine −0.1147	4.3
		Ad −0.1166	2.7

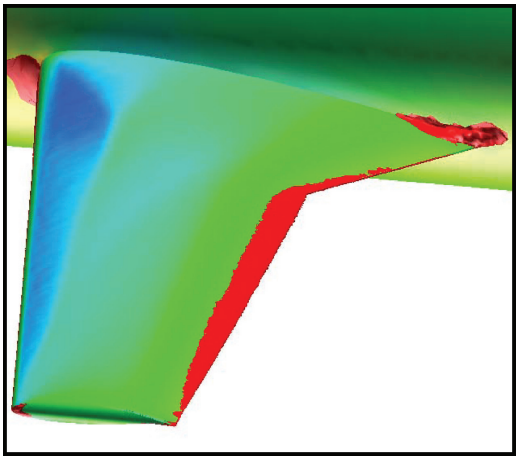

Fig. 15 Separated region show in red. Surface contours of pressure.

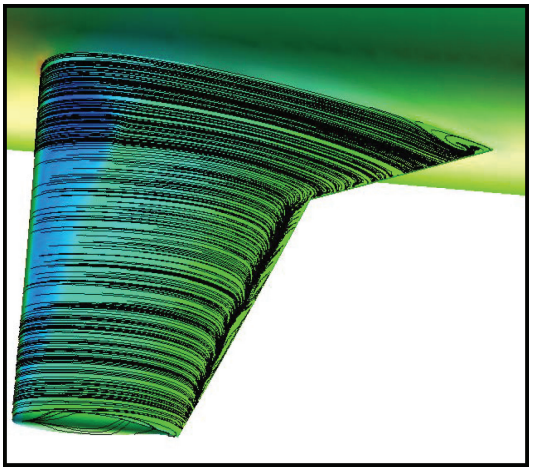

Fig. 16 Oil flow on wing. Surface contours of pressure.

in all three velocity vectors. The oil flow in Fig. 15 confirms the three-dimensionality of the flow at the trailing edge. This separation extends approximately 15% upstream from the trailing edge, impacting the shock location, increasing the pressure drag, and decreasing the skin friction.

The WBNP single-point convergence data for the fine and adapted grids at $\alpha = 1.00$ deg are presented in Table 6. The experimental α for $C_L = 0.50$ is 1.00 deg, and the computationally predicted α is 0.91 deg following a similar procedure to the WB configuration.

The C_L, C_D, and C_M data at a range of angles of attack for the WBNP configuration are presented in Figs. 17–19. The C_L, C_D, and C_M values compare within 5% for all angles of attack for the WBNP configuration. At the lower angles of attack, the predicted lift slope is less than the experimental lift slope, whereas the two slopes become similar at angles greater than 0 deg. As is the case with the WB configuration, a comparison of solutions with the experiments improves with grid refinement.

Figures 20–25 depict the C_p data at various spanwise stations for the $\alpha = 1.00$ deg case. Good agreement between the computations

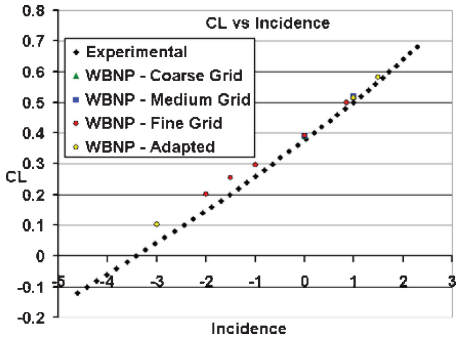

Fig. 17 Plot of C_L vs incidence for the wing-body-nacelle-pylon geometry.

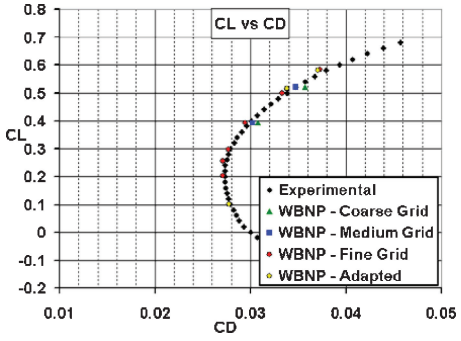

Fig. 18 Plot of C_L vs C_D for the wing-body-nacelle-pylon geometry.

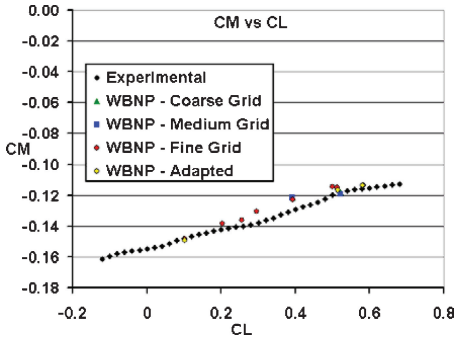

Fig. 19 Plot of C_M vs C_L for the wing-body-nacelle-pylon geometry.

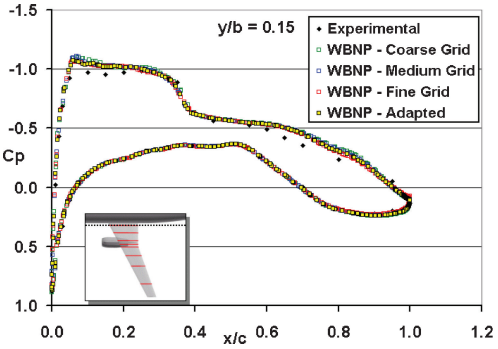

Fig. 20 *Cp* plot at $y/b = 0.15$, $\alpha = 1.0$ deg.

and experiments are observed for all spanwise stations. Again, there appears to be little difference between the three refined grids and the adapted grid. The adapted grid does predict the shock location better and lower C_p values on the upper wing aft of the shock. The major discrepancy is shown in Fig. 22. This station is just inboard of the nacelle and shows the impact of a separation bubble. The refined and the adapted grids produce a larger separation bubble, which is seen in Fig. 26 along with the experimental results. The

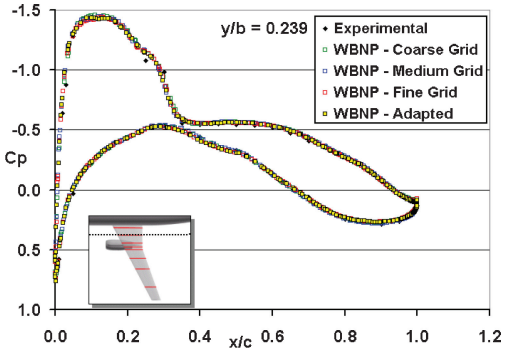

Fig. 21 *Cp* plot at $y/b = 0.239$, $\alpha = 1.0$ deg.

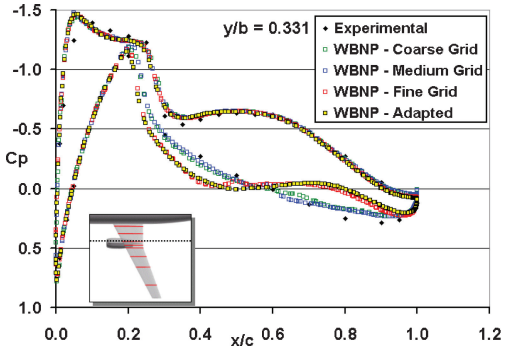

Fig. 22 *Cp* plot at $y/b = 0.331$, $\alpha = 1.0$ deg.

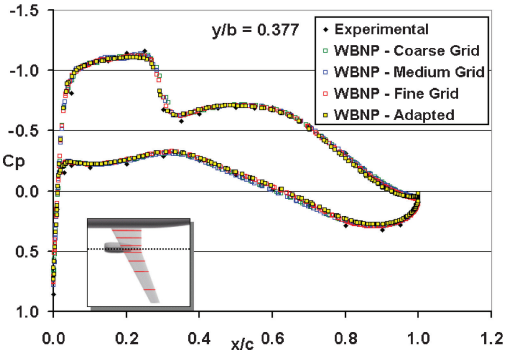

Fig. 23 *Cp* plot at $y/b = 0.377$, $\alpha = 1.0$ deg.

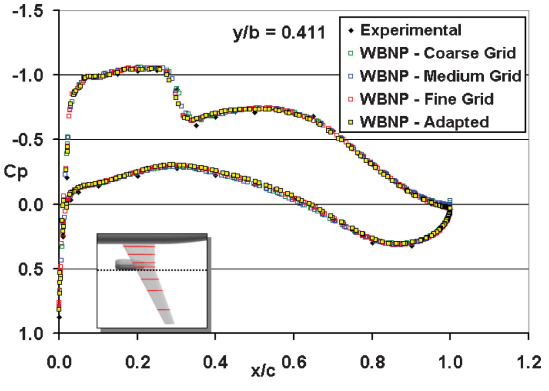

Fig. 24 *Cp* plot at $y/b = 0.411$, $\alpha = 1.0$ deg.

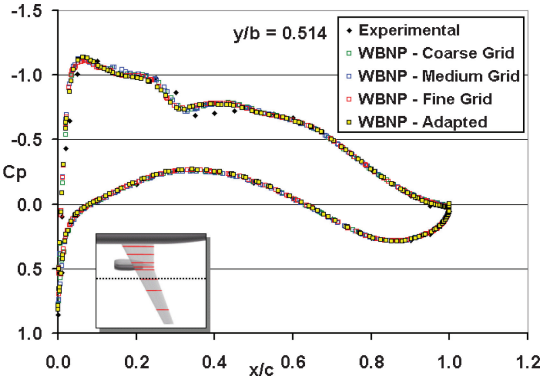

Fig. 25 *Cp* plot at $y/b = 0.514$, $\alpha = 1.0$ deg.

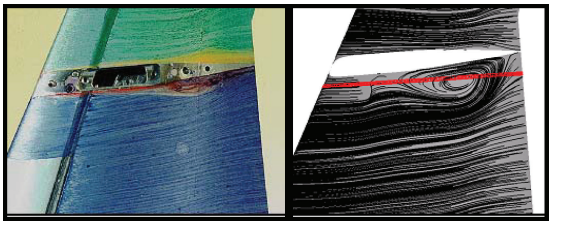

Fig. 26 Experimental and fine-grid oil-flow results. Red line shows pressure taps.

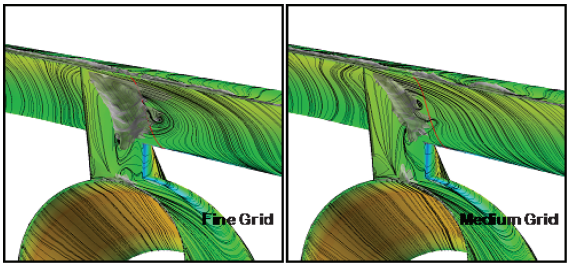

Fig. 27 Isosurface of separated flow for the fine- and medium-grid results. Surface contours of *Cp*.

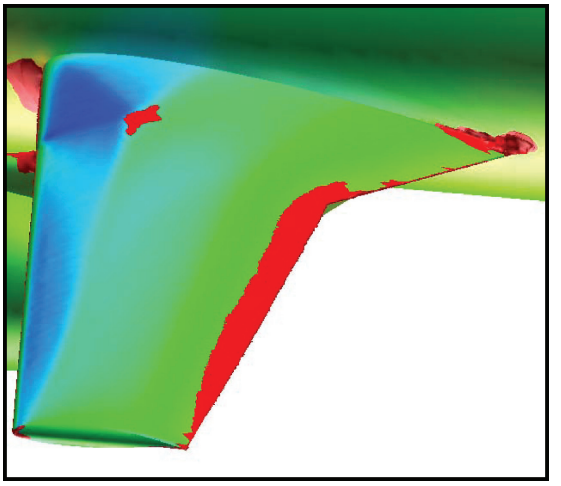

Fig. 28 Separated region show in red. Surface contours of pressure.

experimentally predicted location is inside of the pressure taps and therefore gives the smooth line in the C_p plot. The fine and adapted grids produce a similar curve that cuts through the bubble. Figure 27 shows the extent of the bubble for the fine and medium grids.

A qualitative view of the flow at $\alpha = 1.00$ deg is shown in Figs. 28 and 29 similar to the wing-body results. The separated region at the wing root on the upper side, shown in red in Fig. 28, was documented in the wind tunnel. However, the narrow separated region along the trailing edge has moved forward on the upper surface when compared to the wing-body flow. This separation impacts the shock location and increases pressure drag and decreases skin friction. There is also a separated region on top of the wing over the nacelle caused by shock/boundary-layer interaction. The separated region can clearly be seen in the oil flows as well (Fig. 29).

A vertical view of the flow topology on the upper surface of the wing is shown in Fig. 30. The separated region along the trailing edge is seen on the wind-tunnel model, as is the separated region

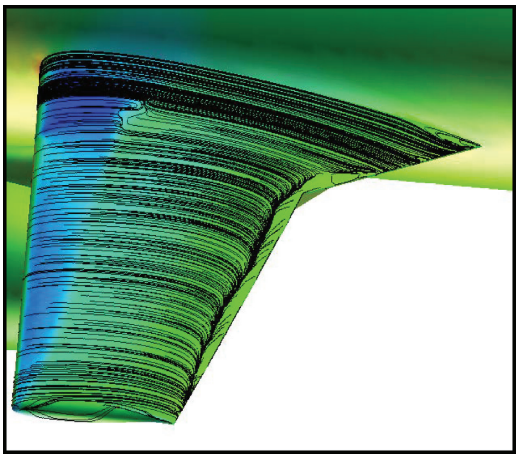

Fig. 29 Oil flow on wing. Surface contours of pressure.

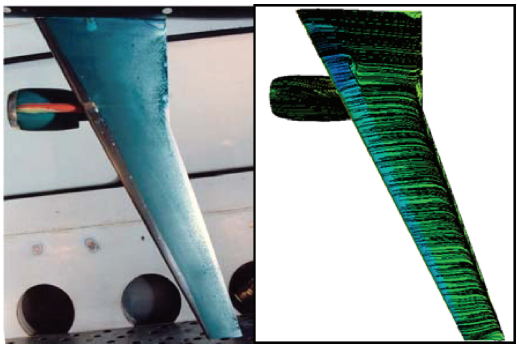

Fig. 30 Experimental and computational oil-flow image of upper wing.

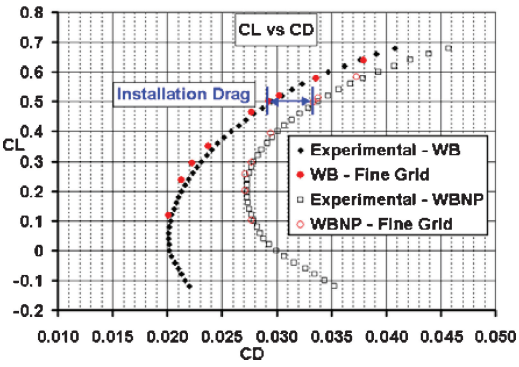

Fig. 31 Installation drag.

at the wing root and wing kink. Simulations that do not capture these phenomena might have difficulty comparing with the integrated quantities in a consistent manner.

The computationally predicted installation drag for $C_L = 0.500$ for the nacelle/pylon combination is 0.0041, and the experimental installation drag is 0.0043 for a difference of 4.6%. The installation drag comparison for the entire range of angles of attack is shown in Fig. 31.

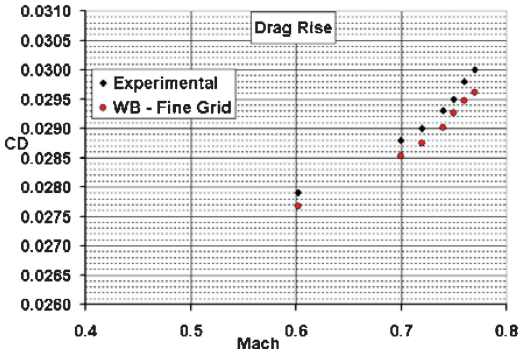

Fig. 32 Wing-body drag rise.

The drag rise for the wing-body configuration was calculated at $C_L = 0.50$ for the Mach-number range (Fig. 32). Reynolds number was held constant, and the simulations were run fully turbulent. Good agreement with the data trend and absolute values was obtained.

Conclusions

The computational-fluid-dynamics (CFD) results computed with Cobalt and just presented have shown that increased accuracy in the prediction of forces and moments on an airliner configuration is possible. These simulations can be achieved by using a computational method that allows complete geometry specification with unstructured grids, a low dissipation solver for accurate answers, and state-of-the-art turbulence modeling for actual wind-tunnel or flight-test condition comparisons. Whereas past uses of CFD have relied on differential calculations to eliminate error sources, current calculations provide absolute comparisons within 5% in C_L, C_D, and C_M, allowing industry to use the method in the design cycle. Additionally, a great amount of insight into the flowfield physics can be obtained by using these methods to investigate regions of separation, caused by vortex, shock, and boundary-layer interactions.

References

[1]Strang, W. Z., Tomaro, R. F., and Grismer, M. J., "The Defining Methods of Cobalt$_{60}$: A Parallel, Implicit, Unstructured Euler/Navier–Stokes Flow Solver," AIAA Paper 99-0786, Jan. 1999.

[2]Tomaro, R. F., Strang, W. Z., and Sankar, L. N., "An Implicit Algorithm for Solving Time Dependent Flows on Unstructured Grids," AIAA Paper 97-0333, Jan. 1997.

[3]Grismer, M. J., Strang, W. Z., Tomaro, R. F., and Witzeman, F. C., "Cobalt: A Parallel, Implicit, Unstructured Euler/Navier–Stokes Solver," *Advances in Engineering Software*, Vol. 29, No. 3–6, 1998, pp. 365–373.

[4]Forsythe, J. R., Strang, W., and Hoffmann, K. A., "Validation of Several Reynolds-Averaged Turbulence Models in a 3D Unstructured Grid Code," AIAA Paper 2000-2552, June 2000.

[5]Gottlieb, J. J., and Groth, C. P. T., "Assessment of Reimann Solvers for Unsteady One-Dimensional Inviscid Flows of Perfect Gases," *Journal of Computational Physics*, Vol. 78, No. 2, 1988, pp. 437–458.

[6]Samareh, J., "Gridtool: A Surface Modeling and Grid Generation Tool," *Proceedings of the Workshop on Surface Modeling, Grid Generation, and Related Issues in CFD Solution*, NASA CP-3291, May 1995, pp. 821–831.

[7]Pirzadeh, S., "Progress Toward a User-Oriented Unstructured Viscous Grid Generator," AIAA Paper 96-0031, Jan. 1996.

[8]Pirzadeh, S., "Vortical Flow Prediction Using an Adaptive Unstructured Grid Method," *Symposium on Advanced Flow Management. Part A: Vortex Flow and High Angle of Attack*, Paper 13, NATO RTO-MP-069(1)-Pt-A, 2001.